

Chapter 23

THz Control in Correlated Electron Solids: Sources and Applications

M. Först, M. C. Hoffmann, A. Dienst, S. Kaiser, M. Rini, R.I. Tobey,
M. Gensch, C. Manzoni and A. Cavalleri

Abstract Materials with strongly correlated electrons often show rich phase diagrams with dramatic differences in physical properties as doping, applied pressure, or magnetic fields are changed. Even subtle perturbations can cause colossal rearrangements in the electronic spectrum, and irradiation with light can be used to drive spectacular rearrangements in the structural, electronic, and magnetic properties. Here, we discuss the use of THz radiation to selectively excite one single degree of freedom at a time to drive a phase change. This is in contrast to what is done in most studies, which achieve photo-induced phase transitions by non-specific excitation in the visible spectral range. This chapter will combine a summary of developments in instrumentation for strong THz fields with some selected scientific applications of THz control of correlated electron systems.

M. Först · M. C. Hoffmann · S. Kaiser · A. Cavalleri (✉)
Max Planck Department for Structural Dynamics,
University of Hamburg - CFEL,
Hamburg, Germany
e-mail: andrea.cavalleri@mpsd.cfel.de

A. Dienst · A. Cavalleri
Department of Physics, Clarendon Laboratory,
University of Oxford, Oxford, UK

M. Rini
Joint Research Centre, European Commission, Karlsruhe, Germany

R.I. Tobey
Optical Condensed Matter Physics, Zernike Institute for Advanced Materials,
University of Groningen, Groningen, The Netherlands

M. Gensch
Helmholtz-Zentrum Dresden-Rossendorf, Dresden, Germany

C. Manzoni
Istituto di Fotonica e Nanotecnologie (IFN) - CNR,
Dipartimento di Fisica, Politecnico di Milano, Milan, Italy

23.1 Introduction

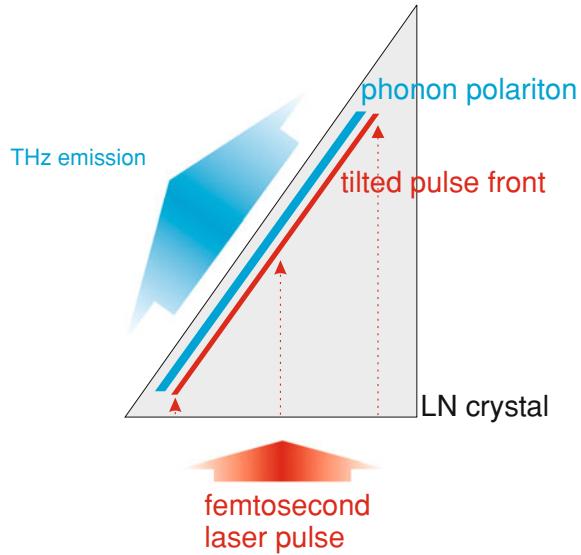
Photo-induced phase transitions are a frontier field in the study of light–matter interaction. In a solid, stimulation with high photon density light can perturb a stable ground state and induce transient metastable phases, often not found near equilibrium. The concept of a photo-induced phase transition is not rigorously defined, but here we refer to any light-simulated non-equilibrium process in which at least one *order parameter* changes. Order may be connected to atomic structural or magnetic symmetries, superconducting or charge-density-wave order or any other type of order that is well-defined near equilibrium. Typically, the states of matter reached through photo-stimulations are also metastable, as they are protected by free energy barriers that make return to the ground state slow, not limited by heat dissipation alone but by cooperative kinetics such as nucleation and growth. Photo-induced phase transitions, as broadly defined above, cover laser-induced melting in semiconductors [1–4], metals [5], semimetals [6, 7], and carbon-based compounds [8–10] and photo-induced dynamics in strongly correlated electron systems.

Solids with strongly correlated electrons are those in which electron–electron interactions, are not any more a perturbation on their kinetic energy, but are comparable or higher and dictate the choice of ground state [11]. Even subtle perturbations in charge occupancy, by chemical doping [12] or excitation with light [13], then cause colossal rearrangements in the electronic spectrum, coupled to the atomic arrangements through electron–phonon coupling. We mention studies of photo-induced phase transitions in magnetoresistive manganites [14–22], non-magnetic oxides like VO₂ [23–32], organic salts [33, 34], charge-density wave dichalcogenites [35–38] or cuprate superconductors [39–43].

In this chapter we focus on one significant new development [44–46], the use of intense mid-infrared or THz pulses to drive phase transitions. As opposed to using eV energy scale excitations, THz radiation can be used to selectively excite one single degree of freedom on low energy scales and to drive a phase change. We will combine a summary of developments in instrumentation with some selected scientific applications. Most of the applications discussed here have been driven by the authors of this work.

The chapter is organized as follows. In Sect. 23.2, we discuss characteristics and generating methods for high-intensity pulses near 1 THz. One application of such pulses is discussed in Sect. 23.2.2, in which the properties of high temperature (high T_c) superconductors are gated at ultrahigh speeds. In Sect. 23.3 we report on the use of mid-infrared radiation to drive bonds in magnetoresistive manganites selectively. A new technique by which high-intensity mid-infrared pulses are generated with a stable carrier envelope phase (CEP) is used to clarify the microscopic mechanism of such nonlinear vibrational control. Finally, we discuss the developments in new sources based on radiation from relativistic electrons.

Fig. 23.1 Schematic for high intensity single cycle THz generation using the tilted-pulse-front technique. Phase matching is achieved by tilting the phase front of the near-infrared pulse, ensuring overlap of the intensity front with the THz field over long distances



23.2 Quantum Phase Control with High-Field THz Pulses

23.2.1 High-Field Single-Cycle Terahertz Pulses: Generation

While broadband single-cycle THz pulses in free space have been available for more than 20 years [47], their pulse energies have typically been far too small to observe nonlinear responses. In this section we will provide an overview of generation methods of intense single-cycle pulses. More detailed discussion can be found in Chap. 14 of this book and in the literature [48].

Optical rectification of mJ-energy femtosecond laser pulses via the tilted-pulse front technique [49] can be used to generate intense THz single-cycle pulses with energies of tens of microJoules and peak field strengths of several hundred kV/cm [50]. This technique is based on the high nonlinear coefficient on stoichiometric LiNbO_3 .

Compared to other nonlinear materials like ZnTe and GaSe this material takes the advantage of having a very large band gap and a high damage threshold. However, due to the large mismatch between optical group index and THz refractive index, efficient phase matching for optical rectification is not possible in this material. To achieve efficient THz output, it is necessary to introduce a noncollinear phase matching scheme by tilting the normal of the intensity front of the femtosecond laser relative to the propagation direction (see Fig. 23.1). For LiNbO_3 the required tilt angle is approximately 63° and can be obtained by using a combination of a reflection grating with an imaging system such as a telescope or lens. The tilted pulse front propagates inside the lithium niobate, and builds up a phonon-polariton

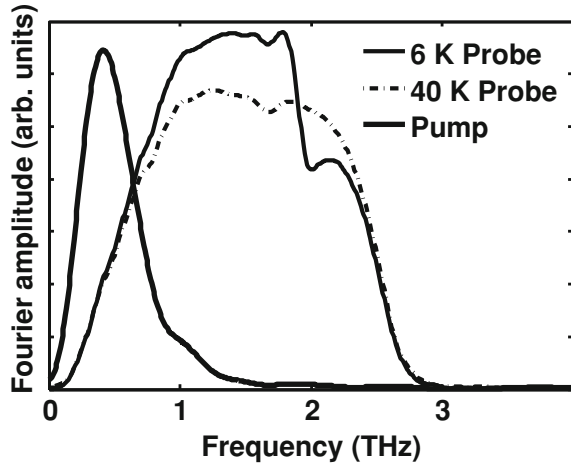
wave [51, 52], which is coherently amplified while being driven by the femtosecond laser. Photorefractive damage in the material can be minimized by using magnesium-oxide doping. The spectrum of the resulting THz pulses extends to about 3 THz and is limited by the intrinsic material absorption of LiNbO_3 close to the lowest optical phonon frequency. The spectral peak is determined by the laser pulse duration and is usually between 0.4 and 1.0 THz. The overall THz generation efficiency can reach values of 10^{-3} . When focused to a diameter of about 1 mm, field peak field strengths of several 100 kV/cm can be achieved.

Another promising technique to obtain single-cycle THz pulses with high field strengths using femtosecond lasers is the generation by nonlinear processes in gas plasmas. THz generation in plasmas has the advantages that there is no damage threshold for the emitter, since the gas target is continuously replenishable, and that the available bandwidth of the THz pulses is essentially limited only by the duration of the pump laser pulse, since no material absorption like optical phonons need to be considered. A large increase in efficiency for THz generation in plasmas was achieved in 2000 by Cook and coworkers [53] through mixing of femtosecond pulses with center frequency ω with their second harmonic at 2ω within the gas plasma. In 2007, Kim et al. reported on pump-to-THz conversion efficiencies exceeding 1×10^{-4} and pulse energies up to $5 \mu\text{J}$ [54]. Ultrabroadband THz pulses containing frequencies up to 100 THz has been demonstrated recently by Thomson by using 19 fs laser pulses [55].

23.2.2 Nonlinear Interlayer Coupling in High T_c Superconductors

Cuprates near optimal doping consist of superconducting planes separated by dielectric layers, forming stacks of intrinsic Josephson junctions and underpinning three-dimensional superconducting transport. The combination of tunneling, which has an equivalent inductive impedance, and capacitive coupling between the planes, leads to collective plasma oscillations of superconducting electrons at terahertz (THz) frequencies, which are typically referred to as Josephson plasma waves [56]. These long-lived, weakly damped oscillations occur because the resistive impedance from non-condensed quasi-particles is, near equilibrium, shorted by the inductor, resulting in LC interlayer electrostatics. Because incident electromagnetic fields couple to the Josephson plasmon, THz spectroscopy provides a useful tool for time- and frequency-domain studies [57, 58]. The plasma wave frequency ω_p near equilibrium is determined by the inductance L and capacitance C , determined by the tunneling and the stacked layers, respectively. The tunneling strength can be modulated by the application of an external magnetic field or voltage [59, 60], possible because tunneling across a weak link depends on the order-parameter phase difference φ between the two superconductors, which is affected by application of external fields [61, 62]. To achieve this effect on the ultrafast timescale, interlayer voltage drops of few to tens of mV are needed, corresponding to THz-frequency transients with peak electric fields of tens of kV/cm.

Fig. 23.2 Fourier amplitude of THz traces reflected from the sample above and below the transition temperature (*thin dashed-dotted and solid curves*). The pump spectrum is shown in comparison as a *thick solid line*



THz pump–THz probe experiments were conducted on $\text{La}_{1.84}\text{Sr}_{0.16}\text{CuO}_4$, an optimally doped compound with $T_C = 36$ K. The sample was excited with high-intensity THz pulses tuned to 400 GHz, well below the 2-THz Josephson plasma resonance.

The peak field reached 100 kV/cm. The pump or gate field, polarized along the c -axis, modulates the quantum mechanical phase difference between adjacent layers, strongly perturbing interlayer coupling between the planes. Probing was achieved with low-fluence pulses generated by optical rectification and detected by electrooptic sampling in Zinc Telluride (ZnTe). Figure 23.2 shows the Fourier amplitude of THz probe traces reflected from equilibrium $\text{La}_{1.84}\text{Sr}_{0.16}\text{CuO}_4$ above and below the transition temperature, representing the development of a frequency-domain plasma edge below T_C for light polarized parallel to the c -axis. The incoming field was also recorded after reflection from a gold-coated portion of the sample.

From the static reflectivity of $\text{La}_{1.84}\text{Sr}_{0.16}\text{CuO}_4$ the complex frequency-dependent c -axis dielectric function $\varepsilon(\omega)$ was extracted by fitting with the two-fluid model [63].

Single-cycle pump pulses centered at 400 GHz were generated by tilted-pulse-front excitation in Lithium Niobate (LiNbO_3), as discussed in Sect. 23.2.1. Pump-probe experiments were performed at 6 K with the pump polarization parallel to the c -axis and field strengths of approximately 100 kV/cm. To extract the transient frequency-dependent dielectric function $\varepsilon(\omega)$ for different pump-probe time delays τ , the amplitude- and phase-resolved probe traces were investigated with a model that considered surface layer of unknown conductivity, over an unperturbed semi-infinite superconductor with the equilibrium optical properties.

The physics of Josephson plasma waves is encapsulated in the loss function, defined as $-\text{Im}(1/\varepsilon(\omega))$. This quantity has a Lorentzian shape and is centered at the Josephson plasma frequency, with a width that is related to damping. The contour plot in Fig. 23.3 depicts the frequency-dependent loss function measured in our experiments as a function of pump-probe time delay.

Fig. 23.3 Contour plot of normalized frequency-dependent loss function as a function of pump-probe time delay τ

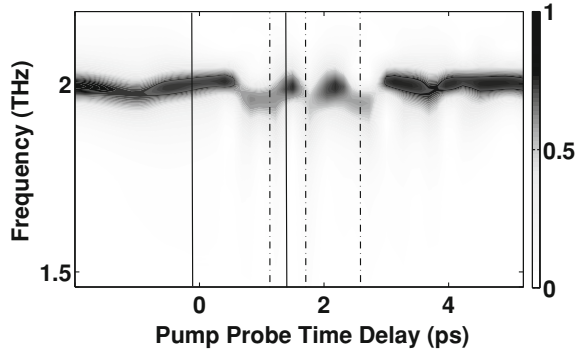
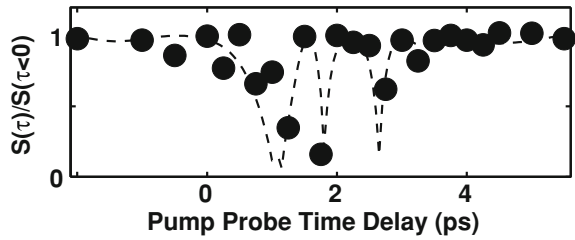


Fig. 23.4 Superconductive transport strength evaluated from experimental data with a fit based on the measured pump field (*dashed line*)



At positive time delays the peak is strongly reduced and shifts toward lower frequencies, indicating a weakening in the plasmonic response. In Fig. 23.4 we display the time-dependent strength of c -axis superconducting transport (dots), evaluated as $S(t) = \lim_{\omega \rightarrow 0} \omega \text{Im}(\sigma(\omega, \tau))$, with σ being the optical conductivity. At equilibrium, this quantity is proportional to the superfluid density ρ_S [64], reflecting interlayer coupling strength in the present case.

To model our experimental observations, we consider the Josephson inductance $L = h/(2eI_C \cos(\varphi_0))$, which depends on the pump-induced phase difference φ_0 and leads to a modulated resonance frequency $\omega_p^* = (LC)^{-1/2} = \omega_p \cos(\varphi_0)^{1/2}$. The normalized superfluid density (dashed-dotted line) deduced in this manner reflects the observed modulation of the loss function and agrees well with the experimentally determined reduction in interlayer coupling $S(t)$. In our picture, the pump field modulates the interlayer coupling by repeatedly driving φ_0 through values of $\pm\pi/2$, at which the inductance diverges as $L \rightarrow \infty$. This is equivalent to a complete decoupling of the layers, at which point transport becomes resistive. At intermediary times, φ_0 is repeatedly driven close to π , leading to a temporary recovery of c -axis transport through inductive coupling.

23.3 Quantum Phase Control Through Vibrational Excitation

23.3.1 Control of the Semicovalent Bond

Manganites are oxides of transition metals typically synthesized in quasi-cubic perovskite structures with formula $RE_{1-x}AE_xMnO_3$, where RE is a trivalent rare earth ion, such as La, Pr, and Nd, and AE is a divalent alkaline earth ion such as Sr and Ca. The RE and AE ions act as charge reservoirs for the manganese ions and control the average Mn charge from 3+ to 4+. The magnetic nature of the Mn-O-Mn bond, in which the sign of the exchange interaction is connected to the size of the electron transfer integral and charge distribution, is responsible for the complexity in these compounds. Typically, “straight” bonds result in ferromagnetic coupling and metallic bonding, while for Mn-O-Mn bonding angles below 180° , insulating phases and anti-ferromagnetic order ensue [65]. Thus, metal–insulator and magnetic transitions can be achieved by changes in doping, application of magnetic fields or pressure.

Among all manganites $Pr_{1-x}Ca_xMnO_3$ is an interesting example, due to its strongly distorted structure. Indeed, the relative radii of Pr and Ca ions differ by a significant amount, leading to large Mn-O-Mn bond angle and small electronic hopping amplitude, which occurs between Mn ions through the bridging oxygen. As a result, this compound shows insulating behavior at all doping levels. For $x = 0.3$ the system is particularly unstable toward a competing metallic phase, which can be induced by the application of magnetic fields [66, 67], electric fields [68], X-ray irradiation [69], laser irradiation, and pressure, resulting in ‘colossal’ changes in the resistivity by up to nine orders of magnitude.

A key parameter is the geometrical “tolerance factor”, Γ defined as:

$$\Gamma = \frac{(A - O)}{\sqrt{2}(Mn - O)},$$

which depends on the average A-O (A=Pr,Ca,La,Sr...) and Mn-O distances. Γ quantifies the degree of orthorhombic distortion from an ideal cubic perovskite symmetry and is related to the Mn-O-Mn bond angle (θ), and hence to orbital overlap and to the transfer integral t between Mn^{3+} and Mn^{4+} sites. The hopping matrix element is maximum for $\Gamma = 1$ (cubic structure, $\theta = 180^\circ$), where metallic behavior is expected, and decreases for smaller angles ($\Gamma < 1, \theta < 180^\circ$), as is the case for symmetry-lowering orthorhombic distortions.

Resonant vibrational excitation can be applied to modulate such tolerance factor. Excitation of IR-active phonon modes can be used to perturb the lattice, changing bond angles and distances selectively. This modifies the overlap of neighboring electronic wavefunctions and the associated electron hopping probability. This concept can be demonstrated by direct excitation of a phonon mode at mid-infrared wavelengths.

Fig. 23.5 Optical conductivity spectrum of $\text{Pr}_{0.7}\text{Ca}_{0.3}\text{MnO}_3$ at low temperature (10 K). The highest frequency mode at $17 \mu\text{m}$ is assigned to the Mn-O stretching vibration

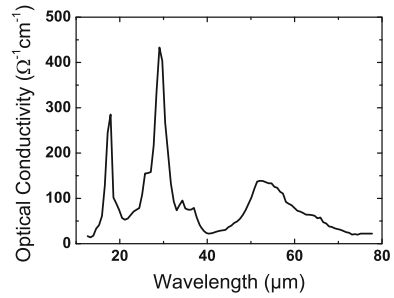
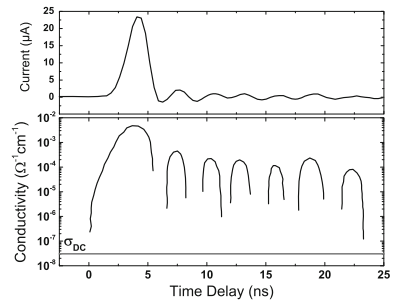


Fig. 23.6 Time-dependent transport measurements, showing that vibrational excitation results in a $\sim 10^3$ increase in the sample current (*upper panel*) and a $\sim 10^5$ increase in the sample conductivity (*lower panel*)



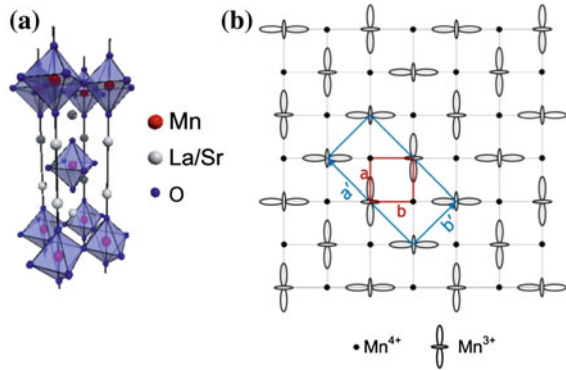
The optical conductivity spectrum of $\text{Pr}_{0.7}\text{Ca}_{0.3}\text{MnO}_3$ shown in Fig. 23.5 exhibits a three-peak structure that is characteristic of most perovskites. The highest frequency IR active mode at $17 \mu\text{m}$ corresponds to the Mn-O stretching vibration, which modulates the tolerance factor Γ and is thus expected to be strongly coupled to the electron system.

High-intensity pulses at this wavelength were generated with an optical parametric amplifier (OPA), pumped by mJ pulses at 1 kHz repetition rate from a titanium sapphire laser. Figure 23.6 displays a prompt, five-order-of-magnitude drop in resistivity following vibrational excitation with femtosecond mid-infrared pulses, generated by difference frequency generation (DFG) between signal and idler. The sample current was monitored with a 4 ns temporal resolution. Experiments were carried out at 30 K, with the sample in the charge-ordered, anti-ferromagnetic insulating phase.

From this, a five-order-of-magnitude change of sample conductivity, from $\sim 3 \cdot 10^{-8} \Omega^{-1} \cdot \text{cm}^{-1}$ to at least $\sim 5 \cdot 10^{-3} \Omega^{-1} \cdot \text{cm}^{-1}$, is estimated. We stress that at the photon energy and laser fluence used in these measurements, both inter-band carrier excitations and laser heating effects could be ruled out as the origin of this resistivity drop. These measurements thus provide evidence that a metallic state is formed promptly by direct vibrational excitation, and that this state persists for hundreds of picoseconds.

To highlight the ultrafast microscopic mechanism underpinning of such dramatic changes in more detail, we investigated the response of $\text{La}_{1/2}\text{Sr}_{3/2}\text{MnO}_4$,

Fig. 23.7 Structure of $\text{La}_{1/2}\text{Sr}_{3/2}\text{MnO}_4$. **a** Three dimensional structure of single layer $\text{La}_{1/2}\text{Sr}_{3/2}\text{MnO}_4$. **b** Below $T_{\text{oo}} = 220$ K, lattice-commensurate ordering of $\text{Mn}3d$ e_g -like orbitals breaks the symmetry of the tetragonal lattice and results in optical birefringence



a half-doped, single-layer manganite in which electronic and orbital structures can be directly connected to the macroscopic optical properties.

Figure 23.7a shows the 3D lattice structure of single-layer $\text{La}_{1/2}\text{Sr}_{3/2}\text{MnO}_4$. The manganese cations occupy the center of oxygen octahedra, and form planes separated by lanthanum and strontium dopants. Within the planes, lattice-commensurate ordering of the high-lying $\text{Mn}3d$ e_g -like orbitals develops below $T_{\text{oo}} = 220$ K, yielding a long-range orbital pattern as shown in Fig. 23.7b. The electronic properties are dominated by the crystal-field-split $\text{Mn}3d$ orbitals, which are strongly hybridized with $2p$ orbitals from neighboring oxygen atoms, and are thus very sensitive to distortions in the Mn-O bond. This low temperature orbital configuration breaks the tetragonal lattice symmetry and results in an optical birefringence—a rotation of the probe polarization when not aligned to either principle axis.

Large amplitude, coherent distortions of the Mn-O bonds were driven with femtosecond pulses at $16 \mu\text{m}$ (625 cm^{-1} , 77 meV) wavelength, resonant with a similar IR-active stretching vibration as the one studied in the cubic $\text{Pr}_{0.7}\text{Ca}_{0.3}\text{MnO}_3$. A second OPA was used to generate broadband probe pulses, which in our experiments were tuned between $10 \mu\text{m}$ (0.12 eV photon energy) and 600 nm (2.2 eV).

The top panel of Fig. 23.8 shows the IR driven time-dependent reflectivity of $\text{La}_{1/2}\text{Sr}_{3/2}\text{MnO}_4$ at 650 nm , measured at a temperature of 90 K , below the orbital ordering temperature. We find a prompt transition to a long-lived phase that survives for hundreds of picoseconds after excitation. The same process probed at other wavelengths in the infrared yielded qualitatively similar temporal profiles. The transient changes in reflectivity, measured at 100 ps time delay, are shown in the middle panel of Fig. 23.2 for photon energies between 120 meV , and 2.2 eV . We observe an increase in reflectivity at all measured photon energies below 1 eV .

The bottom panel of Fig. 23.8 shows the static reflectivity of $\text{La}_{1/2}\text{Sr}_{3/2}\text{MnO}_4$, measured at the $90\text{--}110 \text{ K}$ and at room temperature. Below $T_{\text{oo}} = 220 \text{ K}$, the static reflectivity exhibits a resonance near 1.3 eV , corresponding to intersite excitations between adjacent manganese atoms, reflecting the cooperative, long-range Jahn–Teller distortion. Above T_{oo} , this feature is lost and spectral weight shifts to lower energies. A comparison between reflectivity changes obtained by vibrational

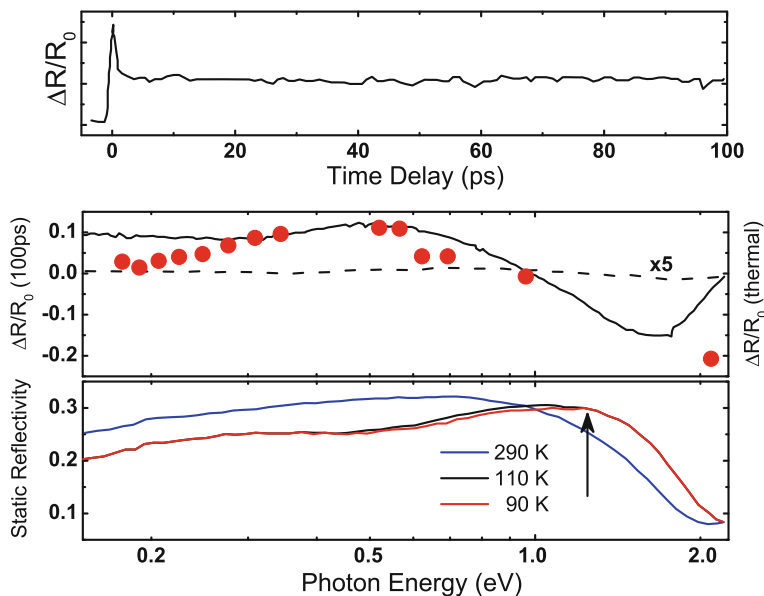
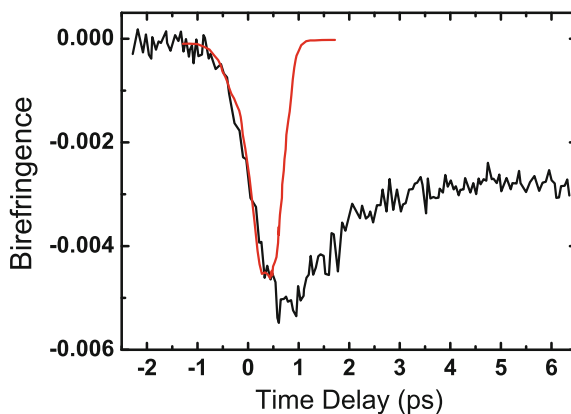


Fig. 23.8 Static and transient reflectivity spectra. (Top) Vibrationally induced changes in reflectivity at 90 K, probed at 650 nm. (Middle) The spectral response at 100 ps time delay (data points) compared to changes in reflectivity when the sample is heated above T_{∞} (solid line) and to sample temperature increased by 20 K (dashed line). (Bottom) The spectral feature at 1.3 eV (arrow) is associated with orbital ordering

Fig. 23.9 Ultrafast loss of birefringence. Excitation of the vibrational resonance at 80 meV results in the prompt destruction of orbital ordering and a loss of birefringence at 650 nm (black). A cross-correlation (red) of the mid-IR pump and 650 nm indicates that melting occurs within the pump pulse



excitation and by static temperature tuning is also shown in the middle panel of Fig. 23.8. We note that the spectral response of the transient phase is the same as the change in static reflectivity when $\text{La}_{1/2}\text{Sr}_{3/2}\text{MnO}_4$ is heated between 90 K and room temperature, suggesting a similarity between the photo-induced phase and the thermally melted orbitally ordered state.

Ultrafast loss of orbital ordering can be directly confirmed by measuring time-dependent birefringence [70], which at 650 nm is proportional to the orbital-order parameter, as measured with resonant X-ray diffraction [71]. Figure 23.9 shows time-dependent birefringence detected at 650-nm after the same vibrational excitation. A prompt drop is observed, directly indicating melting of orbital order. This state persists for hundreds of picoseconds. In Fig. 23.9, we also include a cross-correlation of mid-IR pump and 650-nm probe pulses, as measured by the electro-optic effect in ZnTe. The data show that birefringence is lost on a timescale identical to the rise time of the excitation pulse, indicative of the ultrafast nature of this process. This is an indication that the electronic phase transition is non-thermal, in that it occurs on a timescale that is significantly shorter than the known thermalization time for hot optical phonons in solids [72]. However, the lack of carrier-envelope phase stability results in excitation of lattice vibrations with different absolute phases for subsequent pump pulses, and the signature of the electric field is lost by averaging over many pump-probe cycles.

23.3.2 Mid-Infrared Pulses with Stable Absolute Phase

A very important parameter for the control of a pulse electric field is the CEP, which defines the temporal offset of the peak of the intensity envelope from the carrier wave. For pulses with few-optical-cycle duration, a CEP variation produces a strong change in the waveform. Nonlinear optical processes can be used to measure and manipulate CEP drifts [73], and can be exploited to stabilize it; in particular, difference frequency (DF) mixing between pulses at distinct frequencies, and with carrier-envelope phases φ_1 and φ_2 , give rise to a pulse with absolute phase $\varphi_{\text{DF}} = \varphi_1 - \varphi_2 - \pi/2$. When the two waves are derived from the same laser source or are different components of a broadband pulse, they are mutually phase-locked and $\varphi_1 = \varphi_2 + \Delta\varphi$, where $\Delta\varphi$ is their constant phase difference. The difference frequency process then generates a CE phase stable wave with phase $\Delta\varphi - \pi/2$.

Phase-stable near- and mid-IR pulses have been generated by mixing two spectral portions of a single broadband pulse [74, 75], which are automatically phase-locked THz generation by optical rectification, which produces long wavelength radiation with a stable CEP from an unstable near infrared pulse, as discussed in Par. 2.1, can be understood in these terms [76]. Other schemes for the generation of THz and MIR pulses are based on DFG between two synchronized pulses of different carrier frequencies [77]; in this case, the two pulses follow different optical paths, and fluctuations of their path lengths may influence the CEP of the beam at the DF. The ability to detect and instantaneously correct spurious CEP drifts becomes therefore crucial in phase-sensitive experiments. In the visible and the near IR, f -to- $2f$ interferometry [78] is employed to detect real-time CEP jitter [79, 80].

Here, we discuss a scheme for long-term phase stabilization of MIR pulses, achieved by detecting and compensating its drift [81]. The detection technique is based on the DF mixing between the MIR field (with phase φ_{MIR}) and a gate

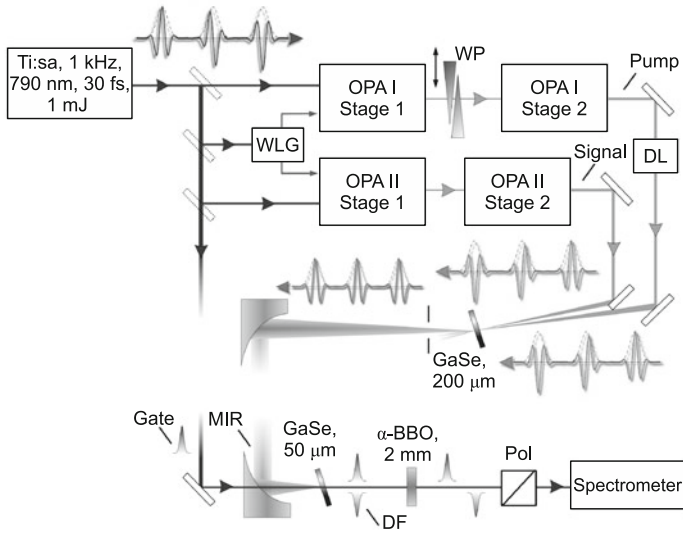


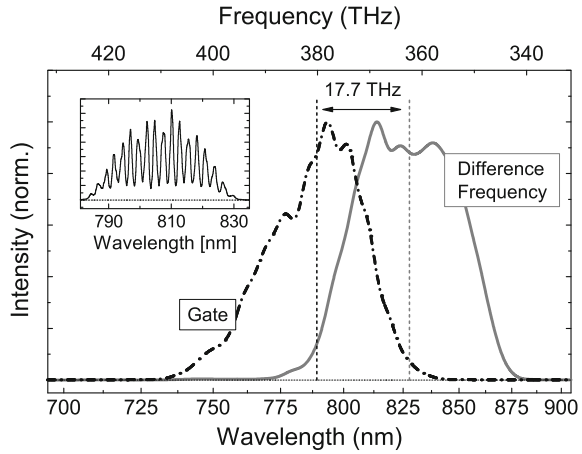
Fig. 23.10 Setup for the production of tunable light pulses at mid-infrared wavelengths (*upper part*) and for the characterization of their absolute phase (*lower part*). WLG is the white-light generation stage; DL is the delay line for Pump-Signal synchronization; WP are fused silica wedge plates; DF is the side-band pulse at the difference frequency

pulse (with phase φ_{Gate}), and on spectral interferometry between the gate and the DF pulse. Due to the difference frequency process, the DF pulses have absolute phase of $\varphi_{\text{Gate}} - \varphi_{\text{MIR}} - \pi/2$: spectral interference between the gate and the DF pulse thus gives rise to a fringe pattern which in the frequency domain has phase $\varphi_{\text{Gate}} - (\varphi_{\text{Gate}} - \varphi_{\text{MIR}} - \pi/2) + \text{const} = \varphi_{\text{MIR}} + \text{const}$. The interference therefore allows single-shot retrieval [82] of the absolute-phase jitter of the MIR pulse, and is independent from the carrier-envelope phase of the gate pulse.

The stable mid-infrared source is displayed in Fig. 23.10, based on two non-collinear two-stage infrared OPAs. The two OPAs are seeded by two portions of the same white light, obtained by self-phase modulation in a 2-mm-thick sapphire plate; this ensures that the OPAs are seeded by phase-locking. The beams from the two OPAs are combined in a 200 μm thick *z*-cut GaSe, oriented for type II DFG; the process provides 2.5- μJ MIR pulses at a wavelength of about 17 μm (≈ 17.6 THz frequency); the DFG process not only shifts the two OPAs to the MIR spectral range, but thanks to the phase-locking of the common seed it provides the key mechanism to produce phase-stable fields. The phase difference $\Delta\varphi$ between pump and the signal pulses can be finely tuned by adjusting their relative path lengths by a fused-silica wedge pair placed before the saturated second stage of OPA I; tuning of $\Delta\varphi$ allows direct control of the CEP of the MIR pulse.

The phase-drift detection is depicted in the lower panel of Fig. 23.10: the MIR pulses are combined with a fraction of the laser source pulses, acting as gate, in a 50- μm thick *z*-cut GaSe crystal for DFG. Their polarizations and the orientation

Fig. 23.11 Spectra of the gate (dash-dotted line), together with the sideband (solid line) arising from difference frequency mixing with the MIR pulses in the GaSe crystal. The weighted center and the corresponding shift is also given. *Inset:* fringe pattern from balanced spectral interference between gate and DF pulses



of the crystal is adjusted for type II [$e(\text{MIR}) + o(\text{DF}) \rightarrow e(\text{Gate})$] interaction. The co-propagating, cross-polarized gate and DF pulses are then delayed to about 1 ps by a 2-mm thick α -BBO plate, projected to the same polarization by an achromatic polarizer and directed to a spectrometer. The DFG process in the thin GaSe crystal is also feasible for EO sampling [83, 84] of the MIR electric field, which allows in situ evaluation of the pulse electric field. In Fig. 23.11 we report the spectra of gate (dash-dotted line) and DF pulses (solid line), together with the fringes arising from their balanced interaction (inset). From the phase of the fringe pattern, the CEP drift of the MIR pulse can be deduced. Figure 23.12 gives an example of short- and long-term characterization of CEP fluctuations of our MIR source. The system exhibits a phase jitter with a root mean square of 80 mrad over 15 s [panel (a)], confirming that DF between two phase-locked beams leads to passive phase-stabilization. However, significant drift can be observed when monitoring the MIR pulses for hours of free-running operation [panel (b)].

This slow drift can be actively compensated by moving the wedge. The data in Fig. 23.12b show that, after the activation of the control system, the MIR absolute phase fluctuations could be compensated, with a residual rms jitter of only 110 mrad.

23.3.3 Vibrational Control as Nonlinear Phononics

The device discussed in Sect. 23.3.2 can be used to further clarify the physics of selective vibrational control in manganites. We first note that linear coupling between the electromagnetic radiation and an infrared-active vibrational mode of the crystal lattice leads to oscillatory atomic motions. However, one expects the lattice to be brought back to rest at the end of the pulse without net work performed. The phase

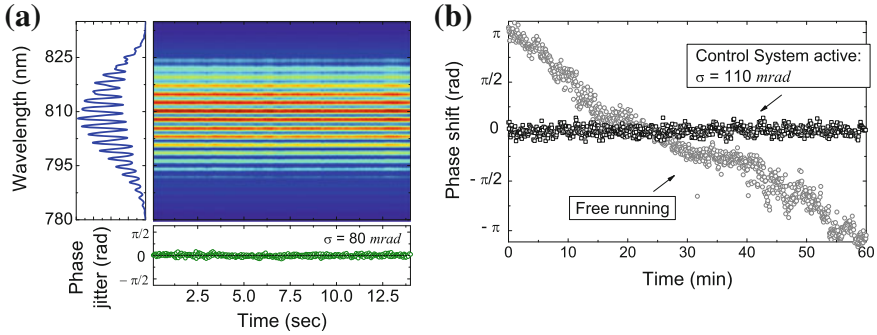


Fig. 23.12 **a** Interferogram recorded for 15 s; the retrieved phase has a jitter of 80 mrad. **b** The same analysis conducted for 1 h: Both free-running and closed-loop measurements are displayed

transition must then be driven by higher order coupling terms, and the physics is difficult to identify without being able to follow the driving field directly.

Similar to the experiments in orbitally ordered $\text{La}_{0.5}\text{Sr}_{1.5}\text{MnO}_4$, single crystals of ferromagnetic-metallic $\text{La}_{0.7}\text{Sr}_{0.3}\text{MnO}_3$ (LSMO) [85–88] were held at 14 K base temperature and excited with mid-infrared radiation at fluences up to 2 mJ/cm^2 . Figure 23.13 shows the time-resolved reflectivity changes for vibrational excitation at $14.3 \mu\text{m}$, resonant with the 75-meV (605 cm^{-1}) stretching mode of MnO_6 octahedra. Similar to what was observed for excitation in the near-infrared, the sample reflectivity decreased during the pump pulse relaxing into a long-lived state, connected to demagnetization of ferromagnetic LSMO [89, 90]. These dynamics are accompanied by coherent phonon oscillations, with frequencies that depend on the excitation wavelength. The Fourier transforms for mid- and near-IR excitation peak at frequencies of the Raman-active rotational E_g mode at 1.2 THz (40 cm^{-1}) and of the rotational A_{1g} mode at 5.8 THz (193 cm^{-1}), respectively [91].

In Figure 23.13b and c, we plot the coherent phonon oscillations and their amplitudes. The amplitude clearly follows the absorption profile of the 75-meV MnO_6 stretching mode, evidencing that the photo-induced dynamics can only be driven when the lattice is distorted.

Nearly 40 years ago, proposals were made of a nonlinear interaction mechanism between a resonantly driven vibration and the crystal lattice, referred to as ionic Raman scattering (IRS) [92, 93]. It was predicted that excitation of an IR-active phonon serves as the intermediate state for a Raman scattering process. In that picture, comparable to optical rectification in nonlinear optics, a rectified phonon field exerts a directional force onto a crystal lattice, inducing an abrupt displacement of the atoms from the equilibrium positions. In the IRS mechanism, the equation of motion of the lattice after infrared excitation can be written as

$$\ddot{Q}_{\text{RS}} + \Omega_{\text{RS}}^2 Q_{\text{RS}} = A Q_{\text{IR}}^2 \quad (23.1)$$

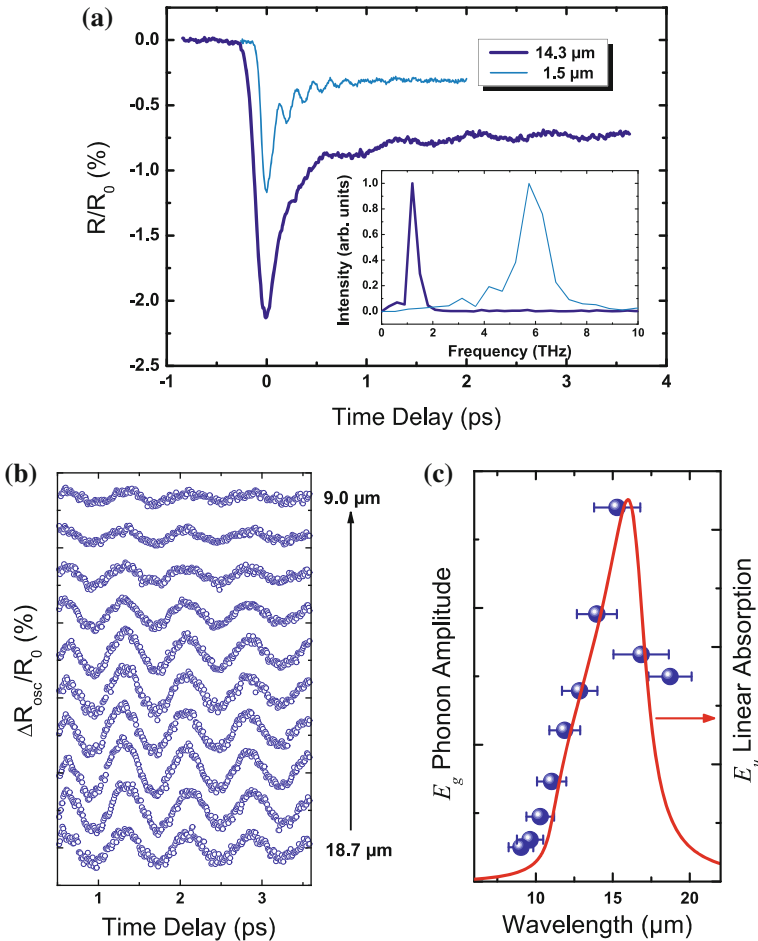
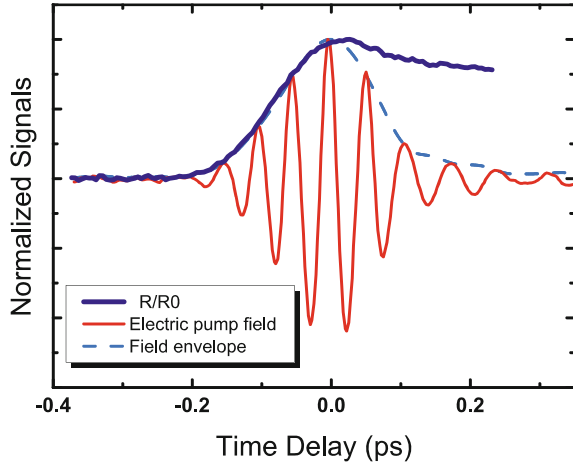


Fig. 23.13 **a** Time-resolved, 800nm-wavelength reflectivity changes of $\text{La}_{0.7}\text{Sr}_{0.3}\text{MnO}_3$ for mid-IR excitation at $14.3 \mu\text{m}$ and for near-IR excitation at $1.5 \mu\text{m}$. The inset shows the Fourier transforms of the oscillatory signal for different pump wavelengths. **b** Coherent phonon oscillations of the E_g mode as a function of the mid-IR pump wavelength. **c** Phonon amplitude derived from these data, together with the linear absorption profile of the IR-active E_u mode

Here, Q_{RS} and Q_{IR} are the coordinates of the low-frequency Raman mode and the resonantly excited high-frequency IR-active mode respectively. The driving force on the right-hand side is second order in the mid-infrared phonon coordinate, and induces a displacive lattice response. Furthermore, only those modes with symmetries belonging to the product group of the infrared vibration are observed, supporting the IRS mechanism. With $E_g \subset E_u \otimes E_u$ for the D_{3d}^6 point group of the distorted perovskite LSMO, and the resonantly excited IR-active mode being of E_u symmetry, this requirement is fulfilled.

Fig. 23.14 Relative change of the sample reflectivity, induced by carrier-envelope phase stable mid-IR excitation in resonance with the MnO_6 stretching vibration (*dark blue solid line*), along with the electric field of the pump pulse measured via electro-optic sampling (*red*)



A second experimental observation substantiates our assignment. Rectification is expected to be independent of the absolute electric field phase of the mid-infrared pump pulses. We excited the system by mid-IR pulses in which the carrier-envelope phase offset was stabilized (see Sect. 23.3.2). Figure 23.14 shows the time-resolved reflectivity rise at the earliest time delays, displayed alongside the carrier-envelope phase-stable pump field, which was measured by electro-optic sampling in a $50\ \mu\text{m}$ thick GaSe crystal.

To increase the temporal resolution, we further used as probe an OPA which delivered broadband IR pulses ($1.2\text{--}2.2\ \mu\text{m}$) compressed to 14 fs. The probe light was spectrally filtered around $1.6\ \mu\text{m}$ in front of the detector. The response of the solid does not show any signature of the phase of the electric field. Instead, the sample reflectivity follows the electric field envelope in agreement with our contention that the driving force results from rectification of the phonon field.

In summary, mid-infrared excitations can stimulate condensed matter through IRS. The key insight is that a rectified phonon field—in analogy to optical rectification in nonlinear optics—can exert a directional force onto the crystal, inducing an abrupt displacement of the atoms from the equilibrium positions. This rectification mechanism could be extended to, e.g., difference-frequency generation between pairs of non-degenerate excitations, opening up avenues for the control of condensed matter with light.

23.4 Undulator-Based Sources for Nonlinear THz Physics

In the previous section, we have shown two examples of the new physics that can be explored with nonlinear THz excitation. We note that tabletop sources are limited in the pulse characteristics in many ways. On the one hand, well-controlled

pulses are generated from the visible to approximately 20- μm wavelength, with pulse energies that decrease at longer wavelengths. The bandwidths are relatively broad, typically exceeding 10%. At longer wavelengths, the availability of strong THz fields is restricted to the few-THz range, below 3 THz for the tilted-pulse-front technique.

Alternative strategies should be developed for high-energy, narrowband THz transients that can be applied to a wide range of nonlinear THz experiments. It is desirable to generate narrow bandwidth and tuneable THz sources in the frequency range between 0.3 and 15 THz, with pulse strengths beyond the 100 μJ range. Electron accelerator sources offer an interesting alternative.

According to the Larmor formula, an accelerated electron radiates [94] with a power $P = 2e^2a^2\gamma^4/(3c)^3$, where e is the elementary charge, a the acceleration, c the speed of light and γ the ratio of the relativistic electron mass to the electron rest mass $\gamma = E/m_0c^2$. Thus, at relativistic energies, the integral radiated power is then increased by a factor γ^4 . If relativistic electrons are passed through an undulator, a periodic magnetic structure that induces a sinusoidal trajectory onto the electrons, tuneable narrow bandwidth radiation can be generated. The spectral bandwidth is determined by the number of undulator periods $\Delta\nu/\nu \sim 1/N_u$ and so is the opening angle of the radiation $\theta_u \sim \sqrt{(1/N_u)}$. The central frequency ν_u of the radiation is tuned by changing the magnetic field strength B [95]. The radiated energy scales linearly with the number of electrons N_e in the bunch and femtoJ—picoJ pulse energies are typically achieved [96].

THz free electron lasers (FELs), operational since the late 1970s, make use of an *optical resonator* to amplify the generated THz power in an undulator [96, 97]. Relativistic electrons serve as both *active laser medium* and *energy pump*. Upon every passage energy is transferred from the electrons to the photons. A few percent of the energy stored in the optical mode is coupled out and few 10 μJ pulse energies can be reached. Most FELs are nowadays driven by radio frequency (RF) accelerators which dictate the upper limit of their repetition rate. The minimum rate is defined by the length of the optical resonator and typically in the MHz regime. Laser-activated switching schemes can be used to reduce the repetition frequency if required [98]. Normal conducting RF accelerators have the drawback that they do not allow to work in continuous wave (cw) operation and only micropulse trains of up to few μs duration are generated with a repetition rate in the few Hz regime [96]. Two of the most recently finalized facilities, the Jefferson Lab FEL [99] and FELBE [100], are based on superconducting RF technology and additionally offer true cw operation at MHz repetition.

A second approach makes use of recent progress of accelerator technology to generate highly charged, ultrashort electron bunches. For frequencies smaller than the inverse electron bunch duration, electrons in a bunch radiate coherently, emitting pulse energies that scale quadratically with the number of electrons N_e . High pulse energies in the few 10 to few 100 μJ regime in the THz frequency range can now be reached already from a single pass through an undulator, since the number of accelerated electrons N_e in a short electron bunch can be of the order of $\sim 10^8$ – 10^{10} and amplification can reach corresponding magnitudes [101]. One such device is

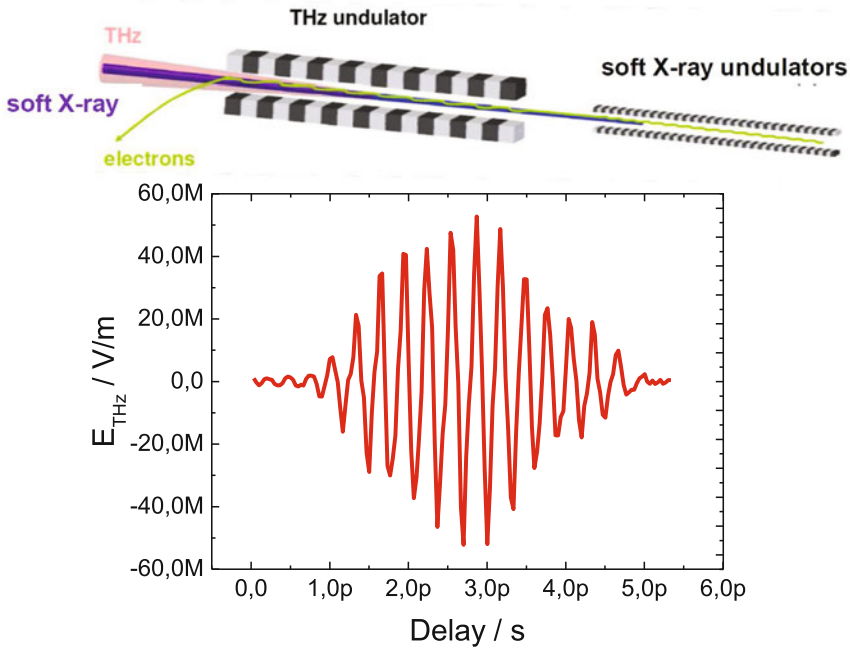


Fig. 23.15 (top) Cascaded design of a soft X-ray undulator followed by a THz undulator at the FLASH facility in Hamburg. The CEP stable THz pulse is fully synchronized to the femtosecond soft X-ray pulse emitted by the same electron bunch as can be seen from the sequential THz/X-ray cross-correlation (for details on the methodology see [103]) of a 3 THz pulse (bottom)

currently in operation, working in parasitic mode at the soft X-ray FEL FLASH in Hamburg [102]. The FLASH THz undulator allows to generate THz pulses with a spectral bandwidth of 10% around the center frequency and additionally provides for intrinsically synchronized THz pump X-ray probe experiments on the few femtosecond timescale (see Fig. 23.15) [103–105].

Similar facilities are currently being developed at the ELBE accelerator in Dresden [106] and at Jefferson laboratory [107]. The facility under construction at ELBE will provide variable repetition rates between 1 and 200 KHz, pulse energies on the 100 μ J level and a tuning range between 0.3 and 3 THz, making this an almost ideal source for THz control experiments.

23.5 Conclusion

The use of high field THz to drive low-lying excitations in complex condensed matter is a field with great potential. The combination of tabletop techniques with accelerator-based sources is proving to bring a healthy balance and new opportuni-

ties. Especially, while on tabletops one has significantly more control on the pulse characteristics, which is exemplified in the exquisite control of the CEP discussed in paragraph 3.2; short pulses and thus few optical cycles are needed to drive the nonlinear optical properties used to manipulate them. As a result, excitation is limited to broad bandwidths and cannot be easily reconnected to narrow-bandwidth, long-timescale couplings that are often of interest in condensed matter research. Second, efficient generation in most nonlinear crystals is limited to frequencies below 3 THz and above 15 THz, due to optical phonon absorption and dispersion. To this end, generation in plasmas can help cover the near-10-THz fraction of the spectrum, although with relatively low fields.

On the other hand, FELs and superradiant accelerator sources allow for long pulses and narrow bandwidths, making it possible to study spectrally selective dynamics on longer timescales. Importantly, accelerator-based sources are generated in non-dispersive vacuum, and thus, all spectral ranges from 1 THz to the near IR are accessible. Yet, control of the pulse characteristics and precise stabilization with external lasers are still challenging.

We mention the pulse energy as an important methodological frontier. At the moment, pulse energies of few μJ are typically available, and a wealth of new studies would become possible if one was able to achieve pulses in the 100 μJ to multi-mJ, exploring the areas of research in which matter is driven further away from equilibrium.

The materials research explored to date covers only a small subset of what is possible. In the future, one will be able to compare the response of selected excitations over a broad section of the electromagnetic spectrum, for example measuring the response of a system to two different vibrations and quantifying the effect that a specific lattice distortion has on the macroscopic properties of a system. Second, spectral and temporal shaping, including the shape of the polarization, will make it possible to dynamically control the lattice parameters via nonlinear phononics as described in Sect. 23.3.3. These techniques will improve our understanding of complex materials and open a new era of controlling the structure of matter.

References

1. C.V. Shank et al., *Phys. Rev. Lett.* **51**, 900 (1983)
2. P. Saeta et al., *Phys. Rev. Lett.* **67**, 1023 (1991)
3. K. Sokolowski-Tinten et al., *Phys. Rev. B* **58**, 11805 (1998)
4. C.W. Siders et al., *Science* **286**, 1140 (1999)
5. B. Siwick et al., *Science* **302**, 5649 (2003)
6. K. Sokolowski-Tinten et al., *Nature* **422**, 287 (2003)
7. D. Sciaini et al., *Nature* **458**, 56 (2009)
8. D.H. Reitze et al., *Phys. Rev. B* **45**, 2677 (1992)
9. A. Cavalleri et al., *Europhys. Lett.* **57**, 281 (2002)
10. S.L. Johnson et al., *Phys. Rev. Lett.* **94**, 057407 (2005)
11. M. Imada, A. Fujimori, Y. Tokura, *Rev Mod. Phys.* **70**, 1034 (1998)
12. Tokura et al., *Rev. Mod. Phys.* (1999)

13. S. Koshihara et al., *Phys. Rev. Lett.* **68**, 1148 (1992)
14. Myano et al., *Phys. Rev. Lett.* **78**, 4257 (1997)
15. M. Fiebig et al., *Science* **280**, 1925 (1998)
16. T. Ogasawara et al., *Phys. Rev. B* **63**, 113105 (2000)
17. R.A. Averitt et al., *Phys. Rev. Lett.* **87**, 017401 (2001)
18. D. Polli, M. Rini, S. Wall et al., *Nature Materials* **6**, 643 (2007)
19. S. Wall et al., *Phys. Rev. Lett.* **103**, 097402 (2009)
20. M. Rini et al., *Phys. Rev. B* **80**, 155113 (2009)
21. P. Beaud et al., *Phys. Rev. Lett.* **103**, 155702 (2009)
22. H. Ichikawa et al., *Nature Materials* **10**, 105 (2011)
23. A. Cavalleri et al., *Phys. Rev. Lett.* **87**, 237401 (2001)
24. A. Cavalleri et al., *Phys. Rev. B* **70**, 161102(R) (2004)
25. A. Cavalleri, H. Chong, S. Formaux, T.E. Glover, P.A. Heimann, B.S. Mun, H. Padmore, J.C. Kieffer, R.W. Schoenlein, *Phys. Rev. B* (Brief report) **69**, 153106 (2004)
26. A. Cavalleri, M. Rini, H. Chong, T.E. Glover, P.A. Heimann, J.C. Kieffer, R.W. Schoenlein, *Phys. Rev. Lett.* **95**, 67405 (2005)
27. M. Rini, et al., *Opt. Lett.* **30**, 558 (2005)
28. M. Rini et al., *Appl. Phys. Lett.* **92**, 181904 (2008)
29. D.J. Hilton et al., *Phys. Rev. Lett.* **99**, 226401 (2007)
30. A. Cavalleri et al., *J. Phys. Soc. Japan* **75**, 01004 (2007)
31. C. Kubler et al., *Phys. Rev. Lett.* **99**, 116401 (2007)
32. M. Rini et al., *Appl. Phys. Lett.* **92**, 181904 (2008)
33. H. Okamoto et al., *Phys. Rev. Lett.* **98**, 037401 (2006)
34. S. Wall et al., *Nature Phys.* **7**, 114 (2011)
35. J. Demsar, L. Forro, H. Berger, D. Mihailovic, *Phys. Rev. B* **66**, 041101 (2002)
36. L. Perfetti et al., *Phys. Rev. Lett.* **97**, 067402 (2006)
37. N. Dean et al., *Phys. Rev. Lett.* **106**, 016401 (2011)
38. S. Hellmann et al., *Phys. Rev. Lett.* **105**, 187401 (2010)
39. R.D. Averitt et al., *Phys. Rev. B* **63**, 140502 (2001)
40. J. Demsar et al., *Phys. Rev. Lett.* **82**, 4918 (1999)
41. R.A. Kaindl et al., *Science* **287**, 470 (2000)
42. N. Gedik et al., *Science* **300**, 1410 (2007)
43. A. Pashkin, M. Porer, M. Beyer et al., *Phys. Rev. Lett.* **105**, 067001 (2010)
44. M. Rini et al., *Nature* **449**, 72 (2007)
45. R.I. Tobey, D. Prabhakaran, A.T. Boothroyd, A. Cavalleri, *Phys. Rev. Lett.* **101**, 197404 (2008)
46. D. Fausti, R.I. Tobey et al., *Science* **331**, 189 (2011)
47. C. Fattinger, D. Grischkowsky, *Terahertz Beams, Appl. Phys. Lett.* **54**, 490 (1989)
48. M.C. Hoffmann, J.A. Fülöp, *J. Phys. D* **44**, 083001 (2011)
49. J. Hebling, G. Almasi, I. Kozma, J. Kuhl, *Opt. Express* **10**, 1161 (2002)
50. K.L. Yeh, M.C. Hoffmann, J. Hebling, K.A. Nelson, *Appl. Phys. Lett.* **90**, 171121 (2007)
51. R.M. Koehl, S. Adachi, K.A. Nelson, *J. Chem. Phys.* **110**, 1317 (1999)
52. T. Feurer, N.S. Stoyanov, D.W. Ward, J.C. Vaughan, E.R. Statz, K.A. Nelson, *Annu. Rev. Mater. Res.* **37**, 317 (2007)
53. D.J. Cook, R.M. Hochstrasser, *Opt. Lett.* **25**, 1210 (2000)
54. K.Y. Kim, A.J. Taylor, J.H. Glowina, G. Rodriguez, *Nature Photon.* **2**, 605 (2008)
55. M.D. Thomson, V. Blank, H.G. Roskos, *Opt. Express* **18**, 23173 (2010)
56. J. Orenstein, A.J. Millis, *Science* **288**, 468 (2000)
57. K. Tamasaku, Y. Nakamura, S. Uchida, *Phys. Rev. Lett.* **69**, 1455 (1992)
58. V.K. Thorsmølle et al., *Opt. Lett.* **26**, 1292 (2001)
59. A.A. Schafgans et al., *Phys. Rev. Lett.* **104**, 157002 (2010)
60. R. Kleiner, P. Müller, *Phys. Rev. B* **49**, 1327 (1994)
61. B.D. Josephson, *Rev. Mod. Phys.* **36**, 216 (1964)
62. B.D. Josephson, *Phys. Lett.* **1**, 251 (1962)
63. S.V. Dordevic et al., *Phys. Rev. Lett.* **91**, 167401 (2003)

64. D.N. Basov et al., *Science* **1**, 49 (1999)
65. J.B. Goodenough, *Phys. Rev.* **100**, 564 (1955)
66. M.V. Zimmermann, J.P. Hill, Doon Gibbs, et al. *Phys. Rev. Lett.* **83**, 4872 (1999)
67. Y. Tomioka, A. Asamitsu, H. Kuwahara, Y. Moritomo, Y. Tokura, *Phys. Rev. B* **53**, R1689 (1996)
68. A. Asamitsu, Y. Tomioka, H. Kuwahara, Y. Tokura, *Nature* **388**, 50 (1997)
69. V. Kiryukhin, D. Casa, J.P. Hill, B. Keimer, A. Vigliante, Y. Tomioka, Y. Tokura, *Nature* **386**, 813 (1997)
70. T. Ogasawara et al., *Phys. Rev B* **63**, 113105 (2001)
71. T. Ishikawa, K. Ookura, Y. Tokura, *Phys. Rev. B* **59**, 8367 (1999)
72. D.V.D. Linde, J. Kuhl, H. Klingenberg, *Phys. Rev. Lett.* **44**, 1505 (1980)
73. A. Baltuška, T. Fuji, T. Kobayashi, *Phys. Rev. Lett.* **88**, 133901 (2002)
74. C. Vozzi, C. Manzoni, F. Calegari, E. Benedetti, G. Sansone, G. Cerullo, M. Nisoli, S. De Silvestri, S. Stagira, *J. Opt. Soc. Am. B* **25**, B112 (2008)
75. R. Huber, A. Brodschelm, F. Tauser, A. Leitenstorfer, *Appl. Phys. Lett.* **76**, 3191 (2000)
76. J. Hebling, K.-L. Yeh, M.C. Hoffmann, B. Bartal, K.A. Nelson, *J. Opt. Soc. Am. B* **25**, B6 (2008)
77. A. Sell, A. Leitenstorfer, R. Huber, *Opt. Lett.* **33**, 2767 (2008)
78. M. Kakehata, H. Takada, Y. Kobayashi, K. Torizuka, Y. Fujihira, T. Homma, H. Takahashi, *Opt. Lett.* **26**, 1436 (2001)
79. R. Zinkstok, S. Witte, W. Hogervorst, K. Eikema, *Opt. Lett.* **30**, 78 (2005)
80. G. Cirmi, C. Manzoni, D. Brida, S. De Silvestri, G. Cerullo, *J. Opt. Soc. Am. B* **25**, B62 (2008)
81. C. Manzoni, M. Först, H. Ehrke, A. Cavalleri, *Opt. Lett.* **35**, 757 (2010)
82. L. Lepetit, G. Chériaux, M. Joffre, *J. Opt. Soc. Am. B* **12**, 2467 (1995)
83. K. Liu, J. Xu, X.C. Zhang, *Appl. Phys. Lett.* **85**, 863 (2004)
84. C. Kübler, R. Huber, S. Tübel, A. Leitenstorfer, *Appl. Phys. Lett.* **85**, 3360 (2004)
85. C. Zener, *Phys. Rev.* **84**, 403 (1951)
86. P.W. Anderson, H. Hasegawa, *Phys. Rev.* **100**, 675 (1955)
87. Y. Okimoto, T. Katsufuji, T. Ishikawa, T. Arima, Y. Tokura, *Phys. Rev B* **55**, 4206 (1997)
88. P.G. Gennes, *Phys. Rev.* **118**, 141 (1960)
89. T. Ogasawara, M. Matsubara, Y. Tomioka, M. Kuwata-Gonokami, H. Okamoto, Y. Tokura, *Phys. Rev. B* **68**, 180407 (2003)
90. R.D. Averitt, A.I. Lobad, C. Kwon, S.A. Trugman, V.K. Thorsmølle, A.J. Taylor, *Phys. Rev. Lett.* **87**, 017401 (2001)
91. E. Granado et al., *Phys. Rev. B* **58**, 11435 (1998)
92. A.A. Maradudin, R.F. Wallis, *Phys. Rev. B* **2**, 4294 (1970)
93. T.P. Martin, L. Genzel, *Phys. Stat. Sol.* (b) **61**, 493 (1974)
94. G.L. Carr et al., *Nature* **420**, 153 (2002)
95. J.A. Clark, *The Science and Technology of Undulators and Wigglers*, (Oxford University Press, New York, 2004)
96. D.A. Jaroszynski et al., *Phys. Rev. Lett.* **71**, 3798 (1993)
97. C.A. Brau, *Science* **239**, 1115 (1988)
98. M.F. Doty et al., *Rev. Sci. Instr.* **75**, 2921 (2004)
99. S. Benson et al., *Nucl. Instr. Meth. A* **582**, 14 (2007)
100. S.A. Zyagin et al., *Rev. Sci. Instr.* **80**, 073102 (2009)
101. B. Faatz et al., *Nucl. Instr. And Meth. A* **475**, 363 (2001)
102. M. Gensch et al., *Infrared Phys. Technol.* **51**, 423 (2008)
103. U. Frähling et al., *Nature Photon.* **3**, 523 (2009)
104. M. Gensch, *AIP Conf. Proc.* **1214**, 19 (2010)
105. F. Tavella et al., *Nature Photon.* **5**, 162 (2011)
106. U. Lehnert et al., *Proceedings of the 32nd International Free Electron Laser Conference*, (Malmö, August, 2010), pp. 23–27
107. S.V. Benson et al., *Nucl. Instr. And Meth. A* (2010). doi:[10.1016/j.nima.2010.12.093](https://doi.org/10.1016/j.nima.2010.12.093)